RESEARCH PAPER

Quantifying the dielectrophoretic force on colloidal particles in microfluidic devices

Roozbeh Abedini-Nassab[1] · Jake Wirfel[2] · Bahram Talebjedi[3] · Nishat Tasnim[3] · Mina Hoorfar[4]

Abstract

We use theory, simulation, and experiment to quantify the dielectrophoretic force produced on spherical colloidal particles exposed to an interdigitated electrode array in a microfluidic environment. Our analytical predictions are based on a simplified two-dimensional model and agree with numerical solutions based on a finite difference scheme. Theoretical predictions align with experimental results without any fitting parameters over a wide range of frequencies and applied voltages. A frequency–response function for negative-dielectrophoresis instruments is derived by developing an equivalent electrical circuit model to understand the system power requirements better. Finally, we investigate the role of electrode width and array spacing on the magnitude and distance dependence of the negative dielectrophoresis force. Our analyses show that the electrode width controls the lateral position of the particles, whereas the voltage controls the vertical position. The strongest forces are achieved when the array spacing is matched to the particle size and when the electrode width is ~1/3 of the array spacing. These results can improve the design and optimization of negative-dielectrophoresis microfluidic instruments for applications in the separation and purification of colloidal microparticles in microelectromechanical systems.

Keywords Negative dielectrophoresis · Microfluidic · Colloidal particles · Interdigitated electrode array · Equivalent circuit model

1 Introduction

The recent advances in microfluidics technology have enabled precise fluid and particle manipulation for various biomedical and chemical analyses on the microscale. The microfluidics techniques have the characteristics of small sample consumption, short reaction time, and low waste generation

Roozbeh Abedini-Nassab and Jake Wirfel contributed equally to this work.

✉ Roozbeh Abedini-Nassab
  abedini@modares.ac.ir

1 Faculty of Mechanical Engineering, Tarbiat Modares University, Tehran 14115-111, Iran

2 Department of Mechanical Engineering and Materials Science, Duke University, Hudson Hall, Box 90300, Durham, NC 27708, USA

3 School of Engineering, University of British Columbia, Kelowna, BC, Canada

4 Department of Mechanical Engineering, University of Victoria, Victoria, BC V8W 2Y2, Canada

rate (Talebjedi et al. 2021a, b). The commonly used microfluidics techniques for particle separation applications include, acoustophoresis (Taatizadeh 2021; Ohiri et al. 2018; Abedini-Nassab et al. 2021), on-chip centrifugation (Nasiri et al. 2020), optical based method (Geiger et al. 2019; Gao et al. 2017; Wang et al. 2021), magnetic technology (Shen and Park 2018; Abedini-Nassab 2019; Abedini-Nassab and Bahrami 2021) and dielectrophoresis separation (Dalili et al. 2021). The dielectrophoresis separation technique stands out as a label-free, non-invasiveness, cost-effective, high throughput and yield compared to conventional particle manipulation methods.

Dielectrophoresis (DEP) refers to a technique of moving electrically polarizable matter with an inhomogeneous electric field. The fundamental idea was introduced by Pohl in the 1950s (Pohl 1951), and has made its way into numerous applications involving the separation and purification of inorganic (Arnold et al. 2006; Krupke et al. 2003; Kullock et al. 2020; Lorenz et al. 2020) organic (Becker et al. 1995; Voldman 2006; Fiedler et al. 1998; Pohl and Hawk 1966; Sang et al. 2016; Yu et al. 2020) and living materials (Green et al. 1997; Hamada et al. 2013; Madiyar et al. 2013). In

addition to DEP, other electrokinetic phenomena, such as AC electro-osmosis (ACEO) (Ramos et al. 1999) and AC electrothermal effects (ACET), (Castellanos et al. 2003), will also induce motion in suspended particles, particularly in fluids of high ionic strength. A discussion of the various electrokinetic phenomena can be found in several review papers (Castellanos et al. 2003; Gascoyne and Vykoukal 2002; Pethig 2010; Gagnon 2011; Ramos et al. 1998), which describe the length, time, and force scales where the different types of phenomena are dominant. DEP is the preferred method for manipulating objects inside microfluidic environments due to the lack of heating and the better spatial control of particles.

There have been several efforts in DEP force prediction through numerical calculations. For example, equations for expressing the acting force on a straight, slender body are proposed (Lin et al. 2009). Also, a theory for calculating the DEP force acting on a chain of spherical particles is suggested (Techaumnat et al. 2004). Moreover, mathematical modeling of the force produced with interdigitated electrode geometry is proposed (Crews et al. 2007).

Though DEP has been the subject of much scientific interest in the field of lab on a chip and microelectromechanical systems (MEMS), there have been surprisingly few attempts to make quantifiable comparisons between experiments and theoretical predictions (Wang et al. 1993; Saucedo-Espinosa and Lapizco-Encinas 2015). Moreover, little attention has been paid to the electrical circuit requirements to hone and optimize the DEP effect. To fill this gap, here we conduct a comprehensive set of experiments and simulations to directly measure the DEP force on colloidal particles in a microfluidic chip over a wide range of field strengths and driving frequencies. We can precisely calibrate the system by employing electrode geometries that can be solved analytically and compared with numerical solutions. The numerical solutions are used to confirm our analytical model. Finally, we develop an equivalent circuit model for the nDEP microfluidic instrument, which can be used to assess the system power requirements, range of operating frequencies, and the optimal chip dimensions for the desired particle manipulation capabilities.

Consistent with prior investigations, here we use interdigitated electrode arrays (IDT), as these geometries can induce strong electric fields throughout the fluid volume (Javanmard et al. 2012; Yan et al. 2014; Albrecht et al. 2004). Prior experiments with IDTs have been conducted with various electrode shapes (e.g., straight bars, saw tooth (Morgan and Green 1997; Sedgwick et al. 2008), square traps (Rosenthal and Voldman 2005), quadrupole traps (Fuhr et al. 1992; Voldman et al. 2003), octupole traps (Schnelle et al. 1993, 2000)) and different modes of excitation (e.g., stationary (Gerard et al. 1997), traveling wave (Cheng et al. 2009), pulsed signals (Cui et al. 2009), and multiple frequencies

(Wang et al. 2009; Urdaneta and Smela 2007)). As our goal is to characterize the DEP force precisely, we limit our analysis to the simplest possible electrode geometry and driving conditions, consisting of an array of rectangular electrodes excited by a sine wave (Fig. 1b). This geometry is ideal because the fields are analytically solvable, and the resulting DEP force is primarily directed towards (or away) from the plane of the electrodes.

We believe that the most reliable characterization method is based on negative dielectrophoresis (nDEP) to repel the particles away from the substrate. Because the DEP force decays exponentially with distance away from the IDT array, the particle will find an equilibrium vertical position where the nDEP force exactly balances that of gravity (Gerard et al. 1997). By measuring these equilibrium positions over a wide range of field strengths and operating frequencies and
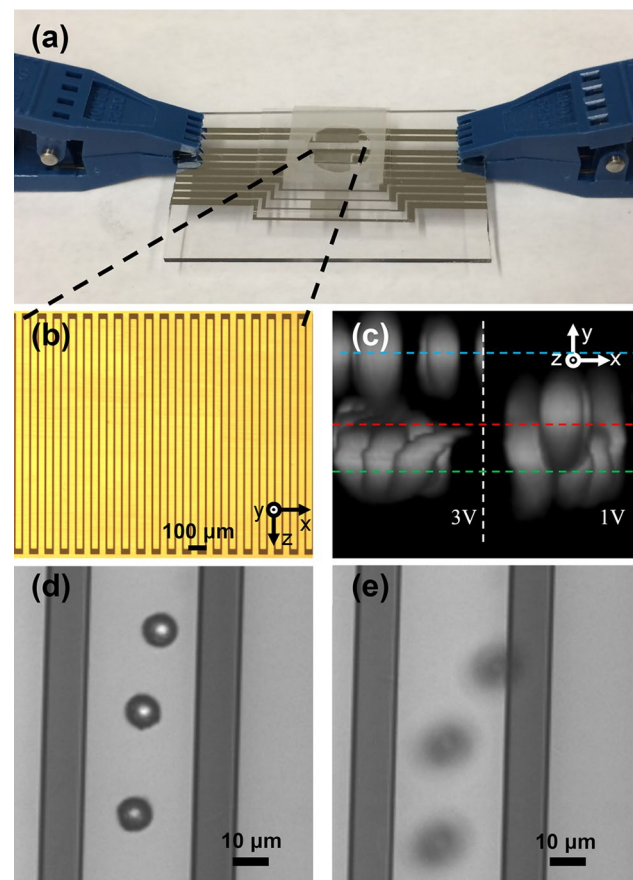
Fig. 1 Experimental setup. The chip and connectors are shown in (**a**) with a magnified view of the electrode array (**b**). A representative confocal microscopy image of beads levitating above the surface is shown in (**c**), where the red and blue dashed lines show the equilibrium position of the beads at 1 and 3 V, as compared to those non-specifically adhered to the substrate depicted by the green dashed line. The applied frequency in these experiments is 1 MHz. Representative brightfield microscopy images show the beads when the applied voltage (peak to peak) is **d** 0V, or **e** 3V

comparing these results against the theoretically predicted locations, it is possible to directly quantify the applied force and determine relevant material properties.

Here, we use a confocal microscope to measure the equilibrium particle locations and then fit the entire data set to estimate the dielectric contrast factor of the particle, also known as the Clausius–Mossotti factor (CM). We believe this approach is preferable to other methods based on the measurement of particle migration velocities in laminar flow fields (Wang et al. 1998) or the holding forces on particles in shear flow (Voldman et al. 2001), which are less easy to calibrate against than gravity.

After carefully calibrating the experimental system, we then analyze the influence of the geometry of the IDT array (i.e., electrode width and array periodicity) on both the magnitude and the distance dependence of the nDEP force. We also develop an equivalent circuit model and plot the frequency–response function for our experimentally tested IDT geometry. This comprehensive theoretical and experimental analysis can serve as a useful guide for designing improved nDEP systems for manipulating colloidal particles inside fluids.

This work, for the first time to our knowledge, provides a good reference for researchers in the field, covering the required information in one place. (i) It presents a new analytical model as well as (ii) numerical simulation results, predicting the nDep behavior, and (iii) confirms the results with experiments. This combination of the three studies and agreements between them without any fitting parameter is rare. (iv) It also provides the practical requirements for running nDEP microfluidic instruments, including the whole nDep system circuit model for enhancing the delivered power to the chip, the IDT geometry design, and the required operational frequencies and voltages. This complete circuit model with the ability to predict the delivered voltages to the chip, to our knowledge, is new, and it is fundamentally required for people in the field to design their nDep systems accordingly.

2 Experimental methods

Figure 1 provides an overview of the experimental system, including a magnified view of the test clips used for electrical connections and the chip (Fig. 1a), a zoomed-in view of the IDT array (Fig. 1b), a representative image of the data obtained in the confocal microscope (Fig. 1c), and a representative bright-field microscopy image of particles levitating above the substrate in the absence (Fig. 1d) or presence (Fig. 1e) of an AC electric field.

Confocal imaging is performed with an upright Zeiss 780 microscope using a 20× objective and a slice width of 0.89μm. Care is taken to level the microscopy stage and

quickly scan through the slices to reduce the amount of bead motion during image acquisition. Measurements are conducted on 30-µm-wide platinum electrodes spaced 10 microns apart. We use two different procedures to determine the separation distance between the bead and substrate depending on the conditions. In one method, we take advantage of the tendency of some beads to non-specifically adhere to the chip surface, which is used as a reference point to measure the relative separation of the nearby levitating beads (see Fig. 1c). When there was an insufficient number of beads adhered to the substrate to generate a reliable measure of separation distance, we employ a second method that uses the image reflections of beads to determine the levitation height. At least ten measurements are collected for each driving frequency and field strength to obtain means and standard deviations. The measurement precision is limited by the slice thickness (here, approximately 1μm).

We ran our experiments in de-ionized water as a low ionic strength fluid. The study was not conducted for higher conductive fluids, such as cell culture media or diluted KCL, which need careful system engineering to minimize ACEO and ACET effects.

3 Theory and simulation

We ran the simulations using our developed custom Matlab codes. To obtain an analytically tractable solution, we develop a 2-D theoretical model for the IDT array, which is a reasonable approximation when the electrode fingers are long (e.g., $\sim 1300\mu$m) compared to the array period (e.g., 40μm). In essence, the potential along the direction of the electrode length is assumed to remain constant (see the coordinate system of Fig. 2a). This problem is easily solved through the separation of variables, subject to suitable boundary conditions.

To find the electric potential, the Laplace equation can be written as $\nabla^2 \varphi = 0$. In this work, the boundary conditions are specified on the electrodes, which are held at potentials, $\pm(V_0/2)\sin(\omega t)$. The electrodes are assumed to be infinitely thin. In between the electrodes, along the boundary of the fluid domain, we assume that the potential is linear and piece-wise continuous, such as that shown in Fig. 2c. Given these assumptions, the electrical potential can be expressed in the Fourier series as

$$\varphi(x,y) = \frac{4V_0}{\pi^2}\left(\frac{L}{L-b}\right)\sum_{n=1}^{N}\frac{1}{n^2}f(n)\sin\left(\frac{n\pi}{L}x\right)e^{-\frac{n\pi}{L}y}, \quad (1)$$

where

$$f(n) = \sin\left(\frac{n\pi}{2}\right)\cos\left(\frac{n\pi b}{2L}\right). \quad (2)$$
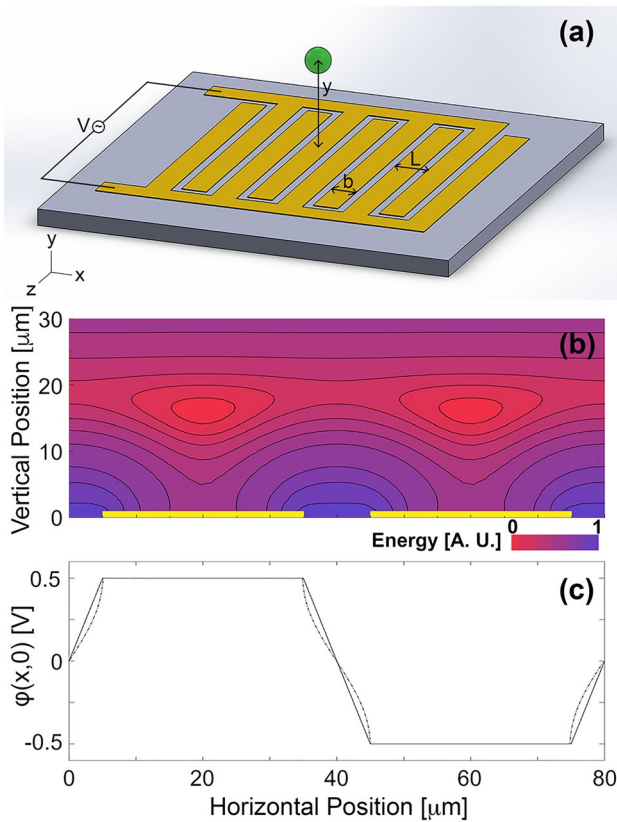
Fig. 2 Schematic of the nDep chip and potential simulation. **a** The negative-dielectrophoresis chip layout is illustrated. The interdigitated electrode array has a period, 2 L, electrode width b, and is connected to an oscillating electrical potential V_0. The particle levitates to a height, y, above the substrate due to the repulsive negative-dielectrophoresis force. **b** The XY-potential energy landscape is depicted for an AC potential 1 Volt (peak to peak), and using the dimensions of our experimental system. The energy minima and maxima are depicted as the red and purple regions, respectively. **c** The solid line depicts the assumed boundary conditions for the analytical solutions, while the dash-dotted line shows the solution obtained from finite difference equations

Equation (2) is a function of the electrode width, b, and the array period, $2L$. What we do here is similar in shape, but different in general, to the one introduced by Morgan and coworkers (Morgan et al. 2001). The electric field distribution is determined from the negative gradient of the electrical potential, given by Eq. (3).

$$\vec{E}(x,y) = \frac{4}{\pi}\left(\frac{V_0}{L-b}\right)\sum_{n=1}^{N}\frac{1}{n}f(n)e^{-\frac{n\pi}{L}y}$$
$$\left[-\cos\left(n\pi xL^{-1}\right)\hat{x} + \sin\left(n\pi xL^{-1}\right)\hat{y}\right],$$
(3)

where $\hat{x}$ and $\hat{y}$ represent the unit vectors in x and y directions, respectively. A solid spherical particle of radius, a, exposed to this field distribution behaves identically as an electric point dipole with a dipole moment (Jones 1995):

$$\vec{p}(\omega) = 4\pi a^3\varepsilon_0 Re\left[\tilde{K}(\omega)\right]\vec{E},$$
(4)

where ε_0 is the dielectric constant of free space, and E is the strength of the electric field at the particle center, while $\tilde{K}(\omega)$ is the frequency-dependent Clausius–Mossotti factor (Jones 1995):

$$\tilde{K}(\omega) = \frac{\tilde{\varepsilon}_p(\omega) - \tilde{\varepsilon}_f(\omega)}{\tilde{\varepsilon}_p(\omega) + 2\tilde{\varepsilon}_f(\omega)}.$$
(5)

The complex electrical permittivity $\tilde{\varepsilon}(\omega)$, is a function of the dielectric permittivity of the particle, ε_p, and fluid, ε_f, and each medium's electric conductivity, σ_p and σ_f, respectively. These properties are related as Eq. (6) (Jones 1995).

$$\tilde{\varepsilon}_{p,f}(\omega) = \varepsilon_{p,f} + j\frac{\sigma_{p,f}}{\omega}.$$
(6)

From Eq. (5), it is clear that the CM factor is thus bounded in the range of $-0.5 \geq \tilde{K}(\omega) \geq 1$. The potential energy of a point dipole exposed to an external electric field is given by Eq. (7).

$$U_e = -\frac{3}{2}\varepsilon_0 V_p Re\left[\tilde{K}(\omega)\right]\vec{E}^2,$$
(7)

where V_p is the volume of the particle. Equation (7) indicates that particles will move towards the local electric field maxima (minima) when the CM factor is positive (negative). Since the CM factor is negative for the particles and frequencies of interest here, the particles tend to move away from the electrodes, causing them to levitate in the y-direction. For this system, the potential energy can be expressed explicitly as (Eq. (8)).

$$U(x,y) = -\frac{24\varepsilon_0\tilde{K}(\omega)V}{\pi^2}\left(\frac{V_0}{L-b}\right)^2\sum_{n=1}^{N}\sum_{m=1}^{N}\left(\frac{1}{nm}\right)$$
$$f(n)f(m)\cos\left(\frac{(n-m)\pi}{L}x\right)e^{-\frac{(n+m)\pi}{L}y},$$
(8)

For one particular IDT array geometry (Fig. 2a, b), in which $b/L = 0.75$, there exists an energy minimum located at $\sim 15\mu m$ above the electrode center. This plot also indicates that a stable vertical position can be achieved by nDEP force alone (i.e., even without the counterbalancing force of gravity). The addition of gravity merely shifts the equilibrium vertical position relative to the nDEP energy landscape. For smaller electrodes, however, the energy minimum is directly in between the electrodes and located at infinity; therefore, gravity is required to achieve a stable equilibrium.

The force acting on the particle is determined by taking the negative gradient of the potential energy represented in Eq. (9).

Table 1 Values used for beads in de-ionized water

Parameter	Value	Parameter	Value
L	$40\mu m$	ε_p	2.60
b	$30\mu m$	σ_f	5.5×10^{-8} S/m
a	$5\mu m$	σ_p	0
ε_0	8.854×10^{-12} F/m	g	9.80 m/s^2
ε_f	78.30	$\Delta\rho$	50 kg/m^3
V_0	0.5V		

$$\vec{F}_e(x, y) = -F_{mag} \sum_{n=1}^{N} \sum_{m=1}^{N} f(n)f(m)e^{-\frac{(n+m)\pi}{L}y}$$
$$\left[\left(\frac{n-m}{nm}\right)\sin\left((n-m)\pi\frac{x}{L}\right)\hat{x} \right. \tag{9}$$
$$\left. +\left(\frac{n+m}{nm}\right)\cos\left((n-m)\pi\frac{x}{L}\right)\hat{y}\right],$$

where F_{mag} is the characteristic magnitude of the dielectric force, and is given by Eq. (10).

$$\vec{F}_{\text{mag}}(x, y) = \frac{24\varepsilon_0 \tilde{K}(\omega)V_p}{\pi L}\left(\frac{V_0}{L-b}\right)^2. \tag{10}$$

When the particle has moved a sufficient distance away from the substrate, the short-range forces from the substrate (e.g., Van der Waals, hydrophobic/hydrophilic interactions) become negligible, and the only remaining long-range force arises from the particle's buoyancy relative to the surrounding fluid (Eq. (11)).

$$F_g = \Delta\rho V_p g. \tag{11}$$

Since the polystyrene beads are denser than the fluid, the net buoyancy force is directed towards the substrate, resulting in a stable equilibrium point when $F_g = F_e$. For notational convenience, it is possible to define a dimensionless quantity that is the ratio of these characteristic force scales (Eq. (12)).

$$\Lambda = \frac{F_{\text{mag}}}{F_g} = \frac{24\varepsilon_0 \left|\text{Re}\left[\tilde{K}(\omega)\right]\right|}{\Delta\rho g\pi L}\left(\frac{V_0}{L-b}\right)^2, \tag{12}$$

where V_0 is set to be 0.5 V for this scaling analysis. As a rough estimate for this system assuming the values in Table 1, the force scale is approximately $\Lambda \approx 10$. Since this parameter is derived from experimental values, it is not considered a fitting parameter.

Due to the strong non-linearity of the dielectric forcing function, it is not possible to obtain an explicit expression of the equilibrium position, y_{eq}, as a function of the system parameters, such as voltage and CM factor. However, it is possible to solve Eq. (10) for V_0 and multiply the numerator

and denominator by the right-hand side and left-hand side of Eq. (11), respectively. Then, by replacing F_{mag}/F_g with Λ (using Eq. (12)), Eq. (13) can be derived.

$$V_0\left(y_{\text{eq}}\right)$$
$$= V_s\sqrt{\sum_{m=1}^{N}\sum_{n=1}^{N}\Lambda^{-1}\left(\frac{n+m}{nm}\right)f(n)f(m)\cos\left((n-m)\pi\right)e^{-\frac{(n+m)\pi}{L}y_{\text{eq}}}}. \tag{13}$$

In the asymptotic limit, where the particle is levitated to distances comparable to the electrode spacing, Eq. (13) can be simplified by retaining the first expansion term only.

$$\frac{y_{\text{eq}}}{a} = \frac{1}{\pi}\frac{L}{a}\left[\ln\left(V_0/V_s\right) - \ln\left(\sqrt{2\Lambda^{-1}}\cos\left(\frac{\pi b}{2L}\right)\right)\right]. \tag{14}$$

Equation (14) predicts that the stable vertical position increases logarithmically with the applied voltage. The first term in the forcing approximation is nearly equal to the numerical solution when the separation distance between the particle and substrate exceeds one particle radius.

The frequency range for which the dielectric force is dominant over other electrohydrodynamic effects can be estimated from the values of Table 1 using the characteristic charge relaxation time scale, $\tau = \varepsilon/\sigma$. The timescale for de-ionized water, with the conductivity of 5.5μS/m, is in the order of a millisecond, implying that the capacitive field associated with dielectrophoresis will dominate at frequencies above 1kHz. On the other hand, in high ionic strength fluids like cell culture media, the timescale is typically on the order of nanoseconds and suggests that nDEP will dominate only at GHz frequencies and beyond.

3.1 Simulation methods

The analytical model of Eqs. (1–3) approximates the electric fields and potentials inside the fluid and is based on an implicit assumption that the surface potential between the electrodes is piecewise and linear. To test the validity of this assumption, we develop a finite difference approach to determine the exact potential in the fluid. Here, we solve the Poisson equation at each point on a square grid having $N \times N$ grid points spaced apart by a distance, h. The equation can be written as $\nabla^2\varphi = \frac{\varphi_{i+1,j}+\varphi_{i-1,j}+\varphi_{i,j+1}+\varphi_{i,j-1}-4\varphi_{i,j}}{h^2} = 0$, where the indices i and j correspond to the x- and y-directions, respectively. For charge-balanced conditions, the solution of the electrostatic potential is thus an arithmetic average of the neighboring grid points, i.e., (Eq. (15)).

$$\varphi_{i,j} = \frac{1}{4}\left(\varphi_{i+1,j} + \varphi_{i-1,j} + \varphi_{i,j+1} + \varphi_{i,j-1}\right). \tag{15}$$

At the chip surface, the potential is only specified on the electrodes as either $+V_0$ or $-V_0$. Meanwhile, for the regions

in between the electrodes, the grid points are solved as Eq. (16).

$$\varphi_{i,0} = \frac{1}{3}\left(\varphi_{i+1,0} + \varphi_{i-1,0} + \varphi_{i,1}\right). \tag{16}$$

Periodic boundary conditions are used along the lateral edges of the container and chosen to satisfy the conditions, $\varphi_{0,j} = \varphi_{N,j}$, $\varphi_{1,j} = \varphi_{N+1,j}$, and $\varphi_{-1,j} = \varphi_{N-1,j}$. The height of the fluid container was chosen to be several array periods in total height, which allows us to specify the upper boundary condition as the far-field approximation of Eq. (1). A grid size of $N = 100h$ was found to achieve numerical convergence, where $h = L/25$.

The solution procedure involves establishing an initial guess for all interior regions of the fluid and then iterating Eqs. (15–16) until the potential reaches convergence. We found that the discrepancy between the analytical and numerical model is relatively small, with the most significant error occurring near the electrode surface (~3.2%). As shown in Fig. 2c, the difference between the approximate piecewise boundary condition and the numerical solution is quite small. It justifies the use of the analytical model to calibrate the experimental apparatus.
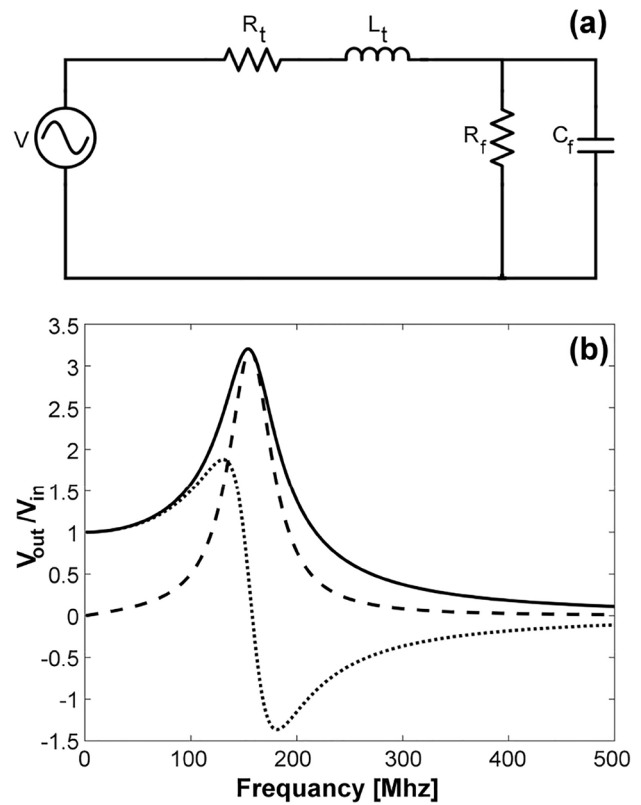
3.2 Equivalent circuit model

Maximizing the nDEP effect requires a circuit design in which most of the voltage is dropped across the fluid. Thus, it is essential to consider the behavior of the experimental system in terms of an equivalent circuit model (Ngo et al. 2014). For example, the capacitance per unit length of the IDT array can be determined from the relationship between the surface charge density and surface voltage on the electrode array. In conductors, one can write $E_n = \sigma(x)/\varepsilon$, where E_n is the normal component of the electric field. Thus, the surface charge density can be determined from the normal component of the electric field as follows:

$$\sigma(x) = \frac{4\varepsilon}{\pi}\left(\frac{V_0}{L-b}\right)\sum_{n=1}^{N}\frac{1}{n}f(n)\sin\left(n\pi x L^{-1}\right). \tag{17}$$

The capacitance per unit area of the interdigitated electrode array can then determine by integrating the total charge on the electrode surface (Eq. 18).

$$C_f = \left(\frac{2\varepsilon A}{L-b}\right)\sum_{n=1}^{N}\frac{f(n)}{(n\pi)^2}\cos\left(\frac{n\pi b}{2L}\right) \tag{18}$$

which for our system amounts to a capacitance of approximately 40 pF for an electrode array of 5 mm². A similar expression can be obtained for the electrical resistance of the electrode array (Eq. 19).

Fig. 3 Equivalent circuit model. **a** In the equivalent circuit model, R_t and L_t represent the resistance and inductance of the wire leads, respectively. R_f and C_f represent the resistance and capacitance of the interdigitated electrodes and the media, respectively. **b** The real part (dotted line), imaginary part (dashed line), and the magnitude of the circuit transfer function are plotted

$$R_f = \left[\left(\frac{2\sigma A}{L-b}\right)\sum_{n=1}^{N}\frac{f(n)}{(n\pi)^2}\cos\left(\frac{n\pi b}{2L}\right)\right]^{-1} \tag{19}$$

which for the same electrode geometry and size is calculated to be 3MΩ when the fluid has a bulk conductivity of deionized water, but only 1 8Ω when the fluid is cell culture media (assuming conductivity of 1S/m).

In addition to the field distribution between the electrodes, there is also a resistance and inductance associated with the wire leads and the impedance of the power supply. The inductance between a pair of wires is computed approximately as

$$L_p = \frac{\mu_0}{\pi}\cosh^{-1}\left(\frac{S}{w}\right), \tag{20}$$

where S is the center-to-center distance between the wires of width, w. The dominant inductance of this circuit is produced by the electrical traces to and from the chip connector, which is estimated to be on the order of $1\mu H$. The diagram

shown in Fig. 3a represents the equivalent circuit of a typical nDEP system. Based on this circuit model, the voltage drop across the fluid is determined by calculating the relative impedance across the fluid compared to that of the entire circuit. For the circuit illustrated in Fig. 3, the transfer function is given as Eq. (21).

$$\frac{V_{\text{out}}}{V_{\text{in}}} = \frac{\left(1 + R_t R_f^{-1} - \omega^2 \omega_R^{-2}\right) - j\omega\left(\omega_L^{-1} + \omega_C^{-1}\right)}{\left(1 + R_t R_f^{-1} - \omega^2 \omega_R^{-2}\right)^2 + \omega^2\left(\omega_L^{-1} + \omega_C^{-1}\right)^2}. \quad (21)$$

The following definitions are used for the characteristic frequencies: $\omega_R = \sqrt{L_t C_f}^{-1}$, $\omega_L = R_f L_t^{-1}$, and $\omega_C = \left(R_t C_f\right)^{-1}$. These characteristic values are associated with the circuit's resonance, inductance, and capacitive time constants. Given our estimated parameters for this circuit, $L_t = 1~\mu H$, $C_f = 40$ pF, $R_f = 3$ MΩ, and using $R_t = 50\Omega$ as the resistance of the co-axial cable and leads, these characteristic frequencies are found to be $\omega_R = 10^8$Hz, $\omega_L = 10^{13}$Hz, and $\omega_C = 10^9$Hz. The real part, imaginary part, and magnitude of Eq. (21) are plotted in Fig. 3b. As seen in this figure, the real part has a peak at ~130Mz and then it drops. That means at frequencies higher than ~130 MHz, the delivered voltage to the chip is lower than the input voltage, and it may not be enough for desired particle levitation. Hence, this analysis suggests that our circuits can operate at frequencies up to tens of MHz, consistent with our experimental results described in Sect. 4. Going beyond these frequencies will require more complicated circuit designs.

4 Results and discussion

The vertical equilibrium positions were measured as a function of the applied voltages of 0–6 V for operating frequencies ranging from 0.1 to 20 MHz. To guide the eye, we also plot the predicted equilibrium positions as a function of the voltage from Eq. (13). The four curves in each plot are calculated based on assumed CM factors of $\tilde{K} = -0.05$, -0.1, -0.3, and -0.5. Overlaid on top of this graph are the predictions of Eq. (14), averaged over the spatial period, $2L$, for considering the minor variation in the vertical force with lateral position. As predicted, the equilibrium position increased logarithmically with voltage. In nearly all instances, the experimental data typically lie between the set of curves with CM factors of -0.3 and -0.5, which is not surprising since $\tilde{K}$ is expected to be near the limit of -0.5 for low dielectric polystyrene beads inside water. To provide a relevant forcing scale, we also introduce another reference axis denoted as "contact force", which represents the calculated force of the bead when in direct contact with the IDT array at each of the corresponding applied voltages. This force is essential since it is the force levitating the particles at rest on the chip. This can be considered as a maximum force that can be applied in different experimental conditions, which for particular IDT array and bead size is in the range of 1–100 pN.

For the highest frequencies tested, ranging from 10 to 20 MHz, the power supply was unable to output the required voltages, which is reflected in the compression of the experimental measurements for these operating conditions. As the experimental data for this frequency regime fall outside expectations, it could also imply that other effects are at play. For our current experimental apparatus, the measurements at frequencies below 10 MHz appear to be most reliable. Thus, to cover the widest range possible for our setup, we focused on frequencies lower than 10 MHz as well as low voltages at 20 MHz.

By comparing the experimental data to theoretical predictions across each dataset of Fig. 4, we provide our best estimate of the fitting values of $K(w)$ as a function of frequency in Fig. 5. The CM factors tend to be around -0.5 for most of the lower frequency range but diverge at frequencies above 10 MHz due to the effects discussed above. The data points for which we have reasonable confidence are plotted as open circles, whereas the remainder is plotted as open diamonds.

The plots in Fig. 5 can also be used for particle separation system design. Since based on these plots, the particles with different CM factors are levitated to different heights, they can predict the separation distance between the particles.

One of the interesting design questions for nDEP systems is determining the optimal geometry for specific particle sizes. For example, manipulating 100 nm diameter virus particles, which experience weak DEP forces, would require a different type of electrode spacing than manipulating 10–20 μm diameter mammalian cells. From Eqs. (9–10), it is clear that the forcing function varies exponentially with the dimensionless ratio of the particle size relative to the electrode period. Thus, the maximum force will be achieved when the IDT array spacing is commensurate with the particle size (see the dashed line of Fig. 6).
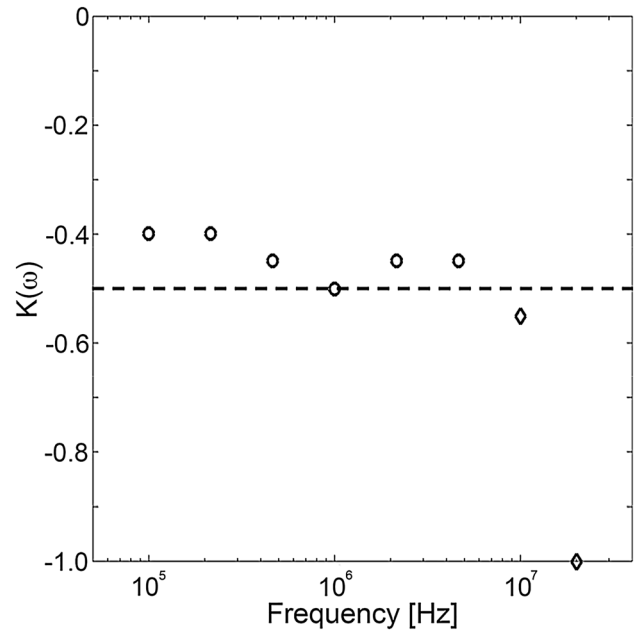
On the other hand, when the electrode spacing is much larger than the particle size, such as in our experiments, the contact force is lower at the surface; however the force is longer ranged. Thus, if the goal is better controlling the vertical position of the bead, it is recommended to use a larger array period. Whereas if the goal is to remove non-specifically adhere beads, it is recommended to use electrodes matched to the particle size to achieve the largest forces.

The other geometric parameter that we analyzed is the ratio of the electrode width relative to the array period (b/L). Figure 7 plots the distance-dependent force profile for different ratios of b/L values, including our experimental ratio of
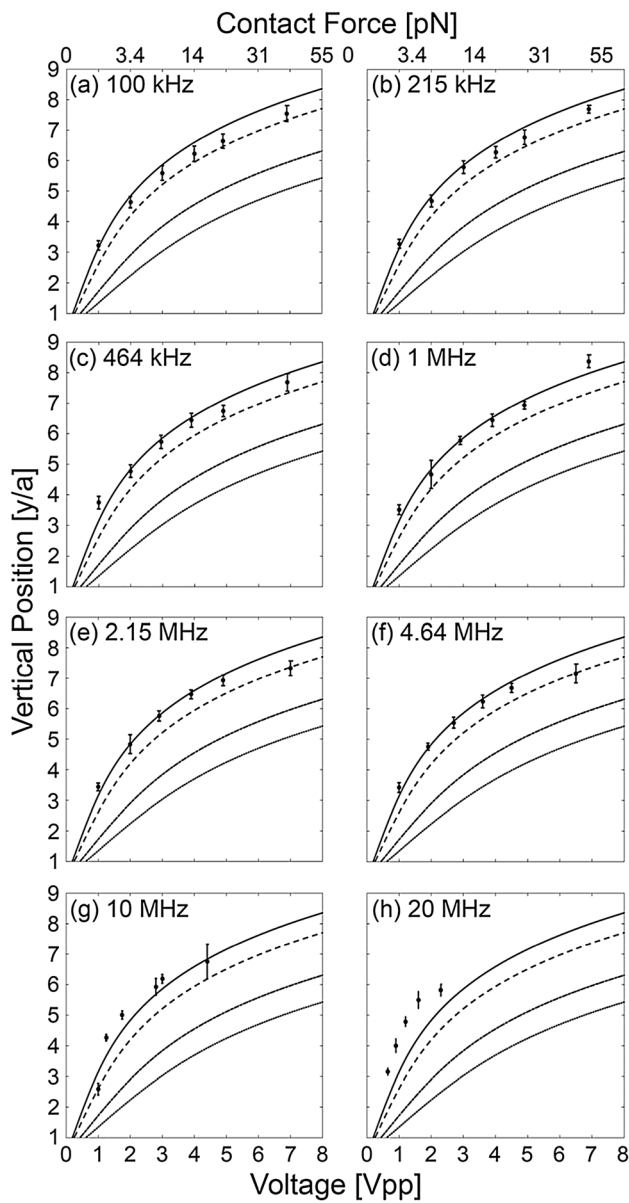
Fig. 4 Particle levitation measurement together with its theoretical predictions. The average vertical position and standard deviation of particles floating in water are plotted as a function of the applied voltage and for different frequencies of **a** 100 kHz, **b** 215 kHz, **c** 464 kHz, **d** 1 MHz, **e** 2.15 MHz, **f** 4.64 MHz, **g** 10 MHz, and **h** 20 MHz. The figure axis labeled "Contact Force" is used to indicate the magnitude of the force that the beads would experience when resting on the substrate for the different applied voltages. The theoretical curves show the predicted equilibrium positions for different Clausius–Mossotti factor having values of −0.5 (solid line), −0.3 (dashed line), −0.1 (dashed-dotted line), and −0.05 (dotted line)
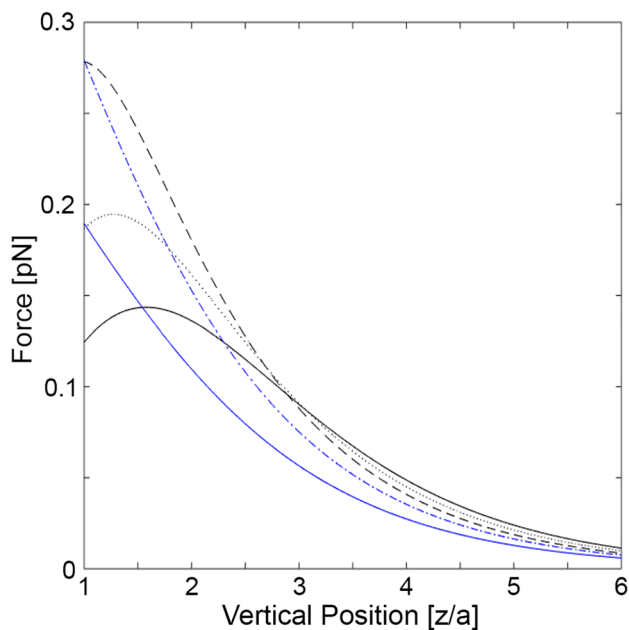

Fig. 5 Clausius–Mossotti factor estimates. Based on the experimental data of Fig. 4; the best fitting Clausius–Mossotti factor is provided. Below 10 MHz, the Clausius–Mossotti factor is estimated to be in the range of −0.4 to −0.5, in good agreement with theoretical expectations (see open circle data points). Data above 10 MHz (indicated by open diamond data points) do not fit with the expected negative dielectrophoresis model
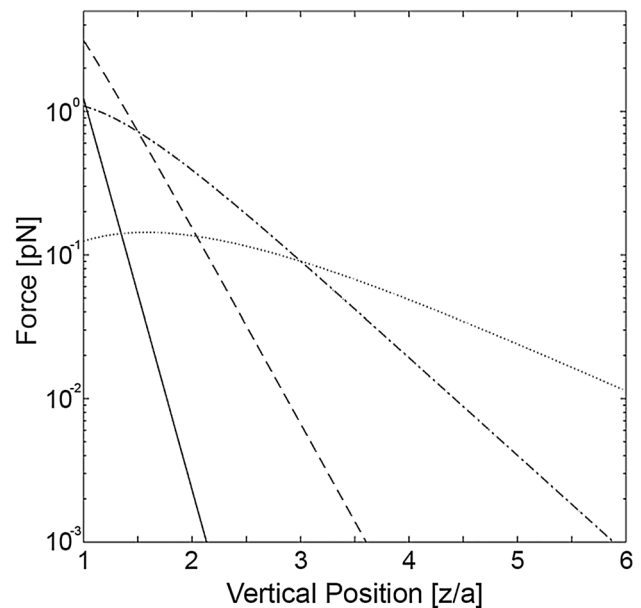
Fig. 6 Forcing profile of various interdigitated electrode array geometries. The force on a $10\,\mu$m diameter particle is plotted as a function of the dimensionless separation distance for substrate periods of $L = 5\,\mu$m (solid line), $10\,\mu$m (dashed line), $20\,\mu$m (dash-dotted line), and $40\,\mu$m (dotted line). The dotted line corresponds to the experimentally tested conditions. The strongest forces are achieved when the substrate period is commensurate with the particle diameter

0.75. We found that for ratios of $b/L > 0.3$, the equilibrium position is located directly above the center of the electrodes rather than in between the electrodes (see also Fig. 1d). For ratios $b/L < 0.3$, on the other hand, the equilibrium positions are located directly in between the electrodes. To indicate

Fig. 7 The force on a 10 μm diameter particle is plotted as a function of the dimensionless separation distance for different b/L ratios of 0.75 (black solid line), 0.5 (black dotted line), 0.35 (black dashed line), 0.25 (blue dash-dotted line) and 0.10 (blue solid line). The color coding depicts whether the equilibrium position is directly on top of the electrodes (black) or in between the electrodes (blue)

these different lateral equilibrium positions, we use either blue or black coloration in Fig. 7. It should also be noted that as the b/L ratio decreases, the agreement between our analytical and numerical solutions surface is less accurate since the assumption of a piecewise linear electrical potential begins to break down. Regardless, the set of curves in Fig. 7 indicates that the ideal electrode geometry should consist of electrodes widths that are ~1/3 of the array period.

5 Conclusion

Though there are many prior experimental demonstrations of negative dielectrophoresis (nDEP) (Arnold et al. 2006; Pohl and Hawk 1966), as well many theoretical analyses of nDEP (Castellanos et al. 2003; Gascoyne and Vykoukal 2002; Morgan et al. 2001), few prior works have combined theoretical (including analytical and numerical) and experimental analyses to directly quantify the nDEP forces on particles inside microfluidic devices, such as what we did here. To provide a firmer foundation for the nDEP field, we combine analytical models, numerical calculations, and experiments to carefully calibrate the nDEP system. We show that dielectrophoretic forces can be quantified with the nearly perfect agreement between theory and experiment. We also show that the range of operating frequencies can

be adequately predicted from equivalent circuit models of the interdigitated electrode array (IDT) electrode geometry. Using the equivalent circuit model, this study is fundamentally important and provides essential information about the proper operational conditions. Finally, we conduct a theoretical analysis that indicates that the ideal IDT array consists of electrode widths that are ~ 1/3 of the array spacing, which is matched to the intended particle size. The results achieved in this work and the difference between experienced nDEP forces acting on the particles with various sizes or dielectric permittivity can be further used for designing size-specific or permittivity-specific robust nDEP particle separation systems.

Though our experiments are conducted in de-ionized water, which is a low ionic strength fluid, in principle, it should be possible to achieve nDEP in fluids with higher conductivity, such as cell culture media or phosphate-buffered saline. However, achieving this goal will require careful system engineering to minimize AC electro-osmosis and AC electrothermal effects, which can dominate nDEP at frequencies below 1 GHz. Thus, if the goal is to conduct experiments on mammalian cells without significant heating, then the circuits need to be optimized for the GHz range to minimize these other electrokinetic effects. Unfortunately, function generators capable of generating GHz range frequency signals are highly expensive. Additionally, the external circuit surrounding the nDEP chip will have to be carefully tuned to enable their reliable operation at GHz frequencies. Though difficult, we expect that it is still possible to achieve nDEP at higher frequencies. Thus, our results should serve as a useful guide for designing dielectrophoretic particle manipulation microchips for the biological and non-biological research fields.

References

Abedini-Nassab R (2019) Magnetomicrofluidic platforms for organizing arrays of single-particles and particle-pairs. J Microelectromech Syst 28(4):732–738

Abedini-Nassab R, Bahrami S (2021) Synchronous control of magnetic particles and magnetized cells in a tri-axial magnetic field. Lab Chip. https://doi.org/10.1039/D1LC00097G

Abedini-Nassab R, Emami SM, Nowghabi AN (2021) Nanotechnology and acoustics in medicine and biology. Recent Pat Nanotechnol. https://doi.org/10.2174/1872210515666210428134424

Albrecht DR, Sah RL, Bhatia SN (2004) Geometric and material determinants of patterning efficiency by dielectrophoresis. Biophys J 87(4):2131–2147. https://doi.org/10.1529/biophysj.104.039511

Arnold MS, Green AA, Hulvat JF, Stupp SI, Hersam MC (2006) Sorting carbon nanotubes by electronic structure using density differentiation. Nat Nano 1(1):60–65. https://doi.org/10.1038/nnano.2006.52

Becker FF, Wang XB, Huang Y, Pethig R, Vykoukal J, Gascoyne PR (1995) Separation of human breast cancer cells from blood by differential dielectric affinity. Proc Natl Acad Sci USA 92(3):860–864

Castellanos A, Ramos A, González A, Green NG, Morgan H (2003) Electrohydrodynamics and dielectrophoresis in microsystems: scaling laws. J Phys D Appl Phys 36(20):2584

Cheng IF, Froude VE, Zhu Y, Chang HC, Chang HC (2009) A continuous high-throughput bioparticle sorter based on 3D traveling-wave dielectrophoresis. Lab Chip 9(22):3193–3201. https://doi.org/10.1039/b910587e

Crews N, Darabi J, Voglewede P, Guo F, Bayoumi A (2007) An analysis of interdigitated electrode geometry for dielectrophoretic particle transport in micro-fluidics. Sens Actuators, B Chem 125(2):672–679. https://doi.org/10.1016/j.snb.2007.02.047

Cui HH, Voldman J, He XF, Lim KM (2009) Separation of particles by pulsed dielectrophoresis. Lab Chip 9(16):2306–2312. https://doi.org/10.1039/b906202e

Dalili A, Montazerian H, Sakthivel K, Tasnim N, Hoorfar M (2021) Dielectrophoretic manipulation of particles on a microfluidics platform with planar tilted electrodes. Sens Actuators, B Chem 329:129204

Fiedler S, Shirley SG, Schnelle T, Fuhr G (1998) Dielectrophoretic sorting of particles and cells in a microsystem. Anal Chem 70(9):1909–1915

Fuhr G et al (1992) Levitation, holding, and rotation of cells within traps made by high-frequency fields. Biochim Biophys Acta 1108(2):215–223

Gagnon ZR (2011) Cellular dielectrophoresis: applications to the characterization, manipulation, separation and patterning of cells. Electrophoresis 32(18):2466–2487. https://doi.org/10.1002/elps.201100060

Gao D et al (2017) Optical manipulation from the microscale to the nanoscale: fundamentals, advances and prospects. Light Sci Appl 6(9):e17039. https://doi.org/10.1038/lsa.2017.39

Gascoyne PR, Vykoukal J (2002) Particle separation by dielectrophoresis. Electrophoresis 23(13):1973–1983. https://doi.org/10.1002/1522-2683(200207)23:13%3c1973::AID-ELPS1973%3e3.0.CO;2-1

Geiger D, Neckernuss T, Pfeil J, Schwilling P, Marti O (2019) High throughput optical analysis and sorting of cells and particles in microfluidic systems. In: Microfluidics, BioMEMS, and Medical Microsystems XVII, vol. 10875, p. 1087517. International Society for Optics and Photonics, Washington.

Gerard HM, Ronald P, Juliette R (1997) The dielectrophoretic levitation of latex beads, with reference to field-flow fractionation. J Phys D Appl Phys 30(17):2470

Green NG, Morgan H, Milner JJ (1997) Manipulation and trapping of sub-micron bioparticles using dielectrophoresis. J Biochem Biophys Methods 35(2):89–102. https://doi.org/10.1016/S0165-022X(97)00033-X

Hamada R, Takayama H, Shonishi Y, Mao L, Nakano M, Suehiro J (2013) A rapid bacteria detection technique utilizing impedance measurement combined with positive and negative dielectrophoresis. Sens Actuators, B Chem 181:439–445. https://doi.org/10.1016/j.snb.2013.02.030

Javanmard M, Emaminejad S, Dutton RW, Davis RW (2012) Use of negative dielectrophoresis for selective elution of protein-bound particles. Anal Chem 84(3):1432–1438. https://doi.org/10.1021/ac202508u

Jones TB (1995) Electromechanics of particles. Cambridge University Press, Cambridge

Krupke R, Hennrich F, Lohneysen H, Kappes MM (2003) Separation of metallic from semiconducting single-walled carbon nanotubes. Science 301(5631):344–347. https://doi.org/10.1126/science.1086534

Kullock R, Ochs M, Grimm P, Emmerling M, Hecht B (2020) Electrically-driven Yagi-Uda antennas for light. Nat Commun 11(1):115. https://doi.org/10.1038/s41467-019-14011-6

Lin Y, Shiomi J, Amberg G (2009) Numerical calculation of the dielectrophoretic force on a slender body. Electrophoresis 30(5):831–838. https://doi.org/10.1002/elps.200800599

Lorenz M, Weber AP, Baune M, Thöming J, Pesch GR (2020) Aerosol classification by dielectrophoresis: a theoretical study on spherical particles. Sci Rep 10(1):10617. https://doi.org/10.1038/s41598-020-67628-9

Madiyar FR, Syed LU, Culbertson CT, Li J (2013) Manipulation of bacteriophages with dielectrophoresis on carbon nanofiber nanoelectrode arrays. Electrophoresis 34(7):1123–1130. https://doi.org/10.1002/elps.201200486

Morgan H, Green NG (1997) Dielectrophoretic manipulation of rod-shaped viral particles. J Electrostat 42(3):279–293. https://doi.org/10.1016/S0304-3886(97)00159-9

Morgan H, Izquierdo AG, Bakewell D, Green NG, Ramos A (2001) The dielectrophoretic and travelling wave forces generated by interdigitated electrode arrays: analytical solution using Fourier series. J Phys D Appl Phys 34(10):1553–1561. https://doi.org/10.1088/0022-3727/34/10/316

Nasiri R, Shamloo A, Akbari J, Tebon P, Dokmeci MR, Ahadian S (2020) Design and simulation of an integrated centrifugal microfluidic device for CTCs separation and cell lysis. Micromachines 11(7):699

Ngo T-T, Shirzadfar H, Kourtiche D, Nadi M (2014) A planar interdigital sensor for bio-impedance measurement: theoretical analysis, optimization and simulation. J Nano- Electron Phys 6:1011

Ohiri KA, Kelly ST, Motschman JD, Lin KH, Wood KC, Yellen BB (2018) An acoustofluidic trap and transfer approach for organizing a high density single cell array. Lab Chip 18(14):2124–2133. https://doi.org/10.1039/c8lc00196k

Pethig R (2010) Review article-dielectrophoresis: status of the theory, technology, and applications. Biomicrofluidics 4(2):022811. https://doi.org/10.1063/1.3456626

Pohl HA (1951) The motion and precipitation of suspensoids in divergent electric fields. J Appl Phys 22(7):869–871. https://doi.org/10.1063/1.1700065

Pohl HA, Hawk I (1966) Separation of living and dead cells by dielectrophoresis. Science 152(3722):647–649. https://doi.org/10.1126/science.152.3722.647-a

Ramos A, Morgan H, Green NG, Castellanos A (1998) Ac electrokinetics: a review of forces in microelectrode structures. J Phys D Appl Phys 31(18):2338

Ramos A, Morgan H, Green NG, Castellanos A (1999) AC electric-field-induced fluid flow in microelectrodes. J Colloid Interface Sci 217(2):420–422. https://doi.org/10.1006/jcis.1999.6346

Rosenthal A, Voldman J (2005) Dielectrophoretic traps for single-particle patterning. Biophys J 88(3):2193–2205. https://doi.org/10.1529/biophysj.104.049684

Sang S et al (2016) Portable microsystem integrates multifunctional dielectrophoresis manipulations and a surface stress biosensor to detect red blood cells for hemolytic anemia. Sci Rep 6:33626. https://doi.org/10.1038/srep33626

Saucedo-Espinosa MA, Lapizco-Encinas BH (2015) Experimental and theoretical study of dielectrophoretic particle trapping in arrays of insulating structures: effect of particle size and shape. Electrophoresis 36(9–10):1086–1097. https://doi.org/10.1002/elps.201400408

Schnelle T, Hagedorn R, Fuhr G, Fiedler S, Muller T (1993) Three-dimensional electric field traps for manipulation of

cells–calculation and experimental verification. Biochim Biophys Acta 1157(2):127–140

Schnelle T, Müller T, Fuhr G (2000) Trapping in AC octode field cages. J Electrostat 50(1):17–29. https://doi.org/10.1016/S0304-3886(00)00012-7

Sedgwick H, Caron F, Monaghan PB, Kolch W, Cooper JM (2008) Lab-on-a-chip technologies for proteomic analysis from isolated cells. J R Soc Interface 5(Suppl 2):S123–S130. https://doi.org/10.1098/rsif.2008.0169

Shen F, Park J-K (2018) Toxicity assessment of iron oxide nanoparticles based on cellular magnetic loading using magnetophoretic sorting in a trapezoidal microchannel. Anal Chem 90(1):920–927

Taatizadeh E et al (2021) Micron-sized particle separation with standing surface acoustic wave—experimental and numerical approaches. Ultrason Sonochem 76:105651

Talebjedi B, Ghazi M, Tasnim N, Janfaza S, Hoorfar M (2021) Performance optimization of a novel passive T-shaped micromixer with deformable baffles. Chem Eng Process Process Intensif 163:108369

Talebjedi B, Tasnim N, Hoorfar M, Mastromonaco GF, De Almeida Monteiro Melo Ferraz M (2021) Exploiting microfluidics for extracellular vesicle isolation and characterization: potential use for standardized embryo quality assessment. Front Vet Sci 7:1139

Techaumnat B, Eua-arporn B, Takuma T (2004) Calculation of electric field and dielectrophoretic force on spherical particles in chain. J Appl Phys 95(3):1586–1593. https://doi.org/10.1063/1.1637138

Urdaneta M, Smela E (2007) Multiple frequency dielectrophoresis. Electrophoresis 28(18):3145–3155. https://doi.org/10.1002/elps.200600786

Voldman J (2006) Electrical forces for microscale cell manipulation. Annu Rev Biomed Eng 8:425–454. https://doi.org/10.1146/annurev.bioeng.8.061505.095739

Voldman J, Braff RA, Toner M, Gray ML, Schmidt MA (2001) Holding forces of single-particle dielectrophoretic traps. Biophys J 80(1):531–541. https://doi.org/10.1016/S0006-3495(01)76035-3

Voldman J, Toner M, Gray ML, Schmidt MA (2003) Design and analysis of extruded quadrupolar dielectrophoretic traps. J Electrostat 57(1):69–90. https://doi.org/10.1016/S0304-3886(02)00120-1

Wang XB, Huang Y, Holzel R, Burt JPH, Pethig R (1993) Theoretical and experimental investigations of the interdependence of the dielectric, dielectrophoretic and electrorotational behaviour of colloidal particles. J Phys D Appl Phys 26(2):312

Wang XB, Vykoukal J, Becker FF, Gascoyne PR (1998) Separation of polystyrene microbeads using dielectrophoretic/gravitational field-flow-fractionation. Biophys J 74(5):2689–2701. https://doi.org/10.1016/S0006-3495(98)77975-5

Wang L, Lu J, Marchenko SA, Monuki ES, Flanagan LA, Lee AP (2009) Dual frequency dielectrophoresis with interdigitated sidewall electrodes for microfluidic flow-through separation of beads and cells. Electrophoresis 30(5):782–791. https://doi.org/10.1002/elps.200800637

Wang H, Enders A, Preuss JA, Bahnemann J, Heisterkamp A, Torres-Mapa ML (2021) 3D printed microfluidic lab-on-a-chip device for fiber-based dual beam optical manipulation. Sci Rep 11(1):14584. https://doi.org/10.1038/s41598-021-93205-9

Yan S et al (2014) On-chip high-throughput manipulation of particles in a dielectrophoresis-active hydrophoretic focuser. Sci Rep 4:5060. https://doi.org/10.1038/srep05060

Yu ES et al (2020) Precise capture and dynamic relocation of nanoparticulate biomolecules through dielectrophoretic enhancement by vertical nanogap architectures. Nat Commun 11(1):2804. https://doi.org/10.1038/s41467-020-16630-w